SCIENCE CHINA
Chemistry

•COMMUNICATIONS•

https://doi.org/10.1007/s11426-024-1946-7

The first chiral cerium halide towards circularly-polarized luminescence in the UV region

Xinyi Niu[1†], Zhichao Zeng[2†], Zhaoyu Wang[1], Haolin Lu[1], Bing Sun[3], Hao-Li Zhang[3], Yongsheng Chen[4], Yaping Du[2*] & Guankui Long[1*]

[1]*Tianjin Key Lab for Rare Earth Materials and Applications, Renewable Energy Conversion and Storage Center, Smart Sensing Interdisciplinary Science Center, School of Materials Science and Engineering, National Institute for Advanced Materials, Nankai University, Tianjin 300350, China;*

[2]*Tianjin Key Lab for Rare Earth Materials and Applications, Center for Rare Earth and Inorganic Functional Materials, Haihe Laboratory of Sustainable Chemical Transformations, Smart Sensing Interdisciplinary Science Center, School of Materials Science and Engineering, National Institute for Advanced Materials, Nankai University, Tianjin 300350, China;*

[3]*State Key Laboratory of Applied Organic Chemistry, Key Laboratory of Special Function Materials and Structure Design (Ministry of Education), College of Chemistry and Chemical Engineering, Lanzhou University, Lanzhou 730000, China;*

[4]*The Centre of Nanoscale Science and Technology and State Key Laboratory of Elemento-Organic Chemistry, Frontiers Science Center for New Organic Matter, College of Chemistry, Nankai University, Tianjin 300071, China*

Received January 21, 2024; accepted February 1, 2024; published online February 7, 2024

Chiral organic-inorganic hybrid metal halides (OIHMHs) have attracted broader scientific community recently in spin light-emitting diodes, and circularly polarized light-emitting diodes. However, the emission peaks of the reported chiral OIHMHs mainly locate in the visible region, and chiral OIHMH with ultraviolet (UV) circularly polarized luminescence (CPL) has been rarely reported. To fill this gap, cerium, a unique rare-earth (RE) element with tunable luminescence from UV to the visible region owing to the 4f-related electronic transition, was introduced to construct the first RE-based chiral OIHMHs, *R*/*S*-MCC. The chirality is successfully transferred from the chiral organic cations to the inorganic cerium chloride framework in *R*/*S*-MCC, as confirmed by the single crystal structures, circular dichroism, and CPL. The emission spectra of *R*/*S*-MCC are in the UV region, originating from the characteristic d-f transition of Ce^{3+}, which making the Ce-based metal halides are ideal candidates towards CPL light sources in the UV region. Notably, *R*- and *S*-MCC are the first RE-based OIHMHs, also the first chiral metal-halides with UV CPL. Our work opens a new avenue for the development of the chiral OIHMH family towards RE-based chiral OIHMH. The RE-based chiral metal halides couple the unique and superior optical, electrical, magnetic, and spintronic properties of RE elements with chirality could accelerate the development of chiral optoelectronics and spintronics toward real applications.

chiral rare-earth halide, ultraviolet circularly-polarized luminescence, d-f transition, rare-earth halide perovskite, chiral perovskite

Citation: Niu X, Zeng Z, Wang Z, Lu H, Sun B, Zhang HL, Chen Y, Du Y, Long G. The first chiral cerium halide towards circularly-polarized luminescence in the UV region. *Sci China Chem*, 2024, 67, https://doi.org/10.1007/s11426-024-1946-7

With inherent inversion symmetry-breaking structures, chiral organic-inorganic hybrid metal halides (OIHMHs) exhibit numerous fascinating chiral optical [1,2], electrical [3,4], magnetic and spintronic properties [5], including circular dichroism (CD) [6,7], circularly polarized luminescence (CPL) [8,9], magneto-chiral dichroism [10], chiral-

†These authors contributed equally to this work.
*Corresponding authors (email: ypdu@nankai.edu.cn; longgk09@nankai.edu.cn)

phonon-activated spin Seebeck effect [8], and chiral-induced spin selectivity effect [11]. Thus, chiral OIHMHs have been widely investigated recently towards potential applications in circularly polarized light detection [12,13], circularly polarized light sources [14], spin light-emitting diodes [15], chiral optical sensing [16], and biological imaging [17,18]. Among these applications, circularly polarized light source possesses prime importance. However, most of the reported chiral OIHMHs emit CPL in the visible region, with only a few reports on the ultraviolet (UV) region. UV CPL light, which has higher energy than CPL in the visible region, will have promising applications as the circularly polarized light source to excite and investigate the excited chiral optical, electrical, and spintronic properties of chiral materials [19,20]. Moreover, UV CPL has huge potential in three-dimensiaonl (3D) displays [21], chiral catalysis [22], information encryption [23], wireless communication [24], high-density information storage [25], biomedical and forensic applications [26]. Thus, it is necessary and highly needed to develop chiral OIHMHs with UV CPL.

The CPL properties and performances in chiral OIHMHs are determined by the constituent units of the chiral organic cations and inorganic components [27,28]. Although researchers have systematically investigated the crystal structures and CPL of Pb- [29], Sn- [30], In- [31], Sb- [32], Bi- [33,34], Cu- [35], Ge- [8], Mn- [36], Zn- [37], Cd- [38], Fe- [31], Rb- [39], Pd- [40], and Ru- [5] based chiral OIHMHs, most of them exhibit visible-region CPL. Compared with the reported chiral OIHMHs, rare-earth (RE) elements have a rich variety of ion types and more diverse optical properties [41,42]. The unique 4f electron-related emission spectra of RE-based luminescent materials could cover the UV, visible, and infrared spectroscopy (IR) regions [43–45]. Thus, the integration of RE as an inorganic component in chiral OIHMHs could be the most promising option and effective strategy to achieve strong CPL emission in the ultraviolet region.

Among the 17 kinds REs, cerium (Ce) has been widely investigated and employed in various optical fields [46,47], such as Ce^{3+}-doped $LaBr_3$ crystals can be used as high-performance scintillators for X-ray imaging [48,49], Ce^{3+}-doped YAG ($Y_3A_{l5}O_{12}$) has been widely implemented as a phosphor in high-power lighting [50,51], and Ce^{3+}-based luminescent complexes can be utilized to prepare the light-emitting diodes (LEDs) [46,52]. These superior optical properties benefit from the unique parity-allowed d-f transition of Ce^{3+} that can be tuned from UV to the visible regions by introducing different coordinated environments [53,54]. In addition, chiral OIHMHs with adjustable geometries can provide diverse Ce^{3+}-based structures to emit different luminescence signals from the d-f transition. Therefore, the combination of the unique optical and electronic properties of Ce^{3+} with chirality is an optimal choice towards the evolution of UV CPL materials. However, based on the Hard-Soft Acid-Base (HSAB) principle, oxygen-containing ligands (such as H_2O and OH^-) exhibit much stronger coordination capacities than halogen anions [55] thus, chiral OIHMH based on RE is unstable under air and humid conditions [56]. Due to this limitation, not many reports are available on the RE-based OIHMH, and to the best of our knowledge, RE-based chiral OIHMH has not been reported as of now.

Herein, the first RE-based chiral OIHMHs, (*R*/*S*-MBA)$CeCl_4{\cdot}2CH_3OH$ (*R*/*S*-MCC, MBA=α-methylbenzylammounium), were designed and synthesized, along with systematic investigation on their crystal structures, magnetic properties, and chiroptical properties in the UV region. Owing to the successful chirality transfer from the chiral cation to the inorganic cerium chloride framework, these Ce^{3+}-based OIHMHs exhibit symmetry-breaking crystal structures, circular dichroism (CD) and CPL. It is also worth noting that *R*/*S*-MCC displays both paramagnetic property and unique UV CPL emission, and the in-depth work to tune the UV CPL under a magnetic field is undergoing. In summary, our work provides the first RE-based chiral metal halides among 17 kinds of RE elements, also the first chiral metal halides with unique UV CPL (Scheme 1 and Table S1, Supporting Information online), which will accelerate the maturation of chiral OIHMHs with UV CPL emission. The interdisciplinary emerging frontier between the unique chiral optical, electrical, magnetic, and spintronic properties of RE materials with chirality could promote the development of the next-generation UV CPL light source.

The single crystals of *R*/*S*-MCC were synthesized *via* a facile solution method and grown by an antisolvent-assisted crystallization strategy. Single-crystal X-ray diffraction revealed that *R*-MCC and *S*-MCC belong to the triclinic crystal system and crystallize into the asymmetric *Sohncke* space group of *P*1 (CCDC No. 2327202, 2327203) (Table S2). On the contrary, the achiral Ce^{3+}-based metal halides crystallized into the *Pbcm* groups with mirror plane or inverse symmetry centre [57]. As depicted in Figure 1a, the crystal structures of *R*/*S*-MCC are mirror symmetric, and each Ce^{3+} coordinates with six chloride ions and two methanol molecules, forming a distorted dodecahedron. The bond lengths of the dodecahedrons are not equal. The Ce–Cl bond lengths vary from 2.82 to 2.95 Å, and the Ce–O bond lengths vary from 2.49 to 2.54 Å (Tables S3 and S4). This distortion may be related to the chirality transfer caused by chiral cations. The chirality transfer is further supported by the crystallographic indexing based on Wilson statistics and the cumulative intensity distribution, which match well with the acentric curve (Figure S1, Supporting Information online) [58]. The $<|E^2-1|>$ value is 0.763 for both *R*- and *S*-MCC, suggesting their space groups are non-centrosymmetric (Figure S2). As shown in Figure 1a, the edge-sharing dodecahedrons constitute one-

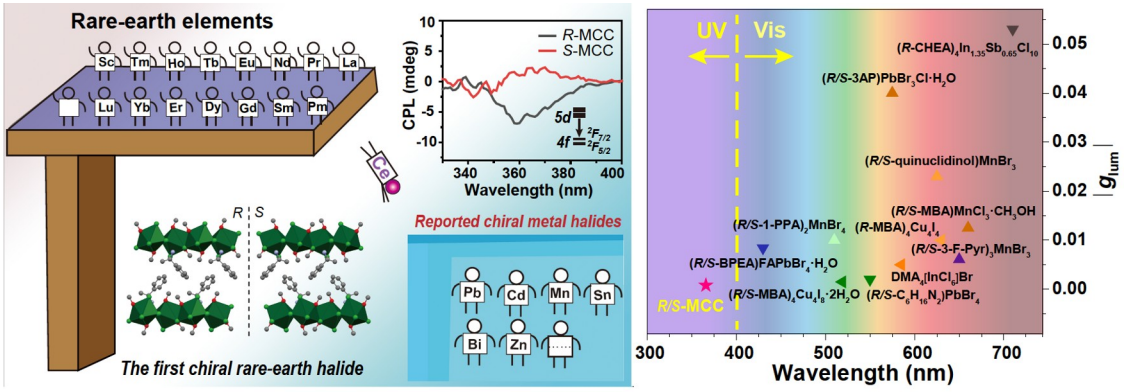

Scheme 1 The first chiral cerium halide, a new family member of chiral organic-inorganic hybrid metal halides, is reported in this work. Comparison between the emission wavelengths and the corresponding values for $|g_{lum}|$ of chiral OIHMHs reported in literatures and this work (color online).

dimensional (1D) chain structure along the *b*-axis. From the perspective of the *b*- or *c*-axes, the inorganic dodecahedrons are not connected, and all the *R*/*S*-MBA cations are distributed around the 1D inorganic chains through hydrogen bonding (Figure S3). The powder X-ray diffraction (PXRD) patterns of the *R*/*S*-MCC samples match very well with those simulated from their single crystals, indicating the as-synthesized samples exhibit high phase purity (Figure 1b, c).

To further analyze the structure of the as-synthesized samples, the Fourier transform infrared (FT-IR) spectroscopy was employed to investigate the vibration of the organo-functional groups in *R*/*S*-MCC (Figure S4). The FT-IR peaks at 1,160 and 1,223 cm^{-1} should be attributed to the C–N vibration absorption related to the chiral centre of *R*/*S*-MBA cations. X-ray photoelectron spectroscopy (XPS) was subsequently employed to investigate the valence and chemical state of each element in the crystal structures of *R*/*S*-MCC (Figures S5 and S6). The XPS peak at approximately 286.37 eV should be ascribed to the carbon atom (C 1s) in the coordinated methanol molecules, while those at 200.3 and 198.7 eV are assigned to the coordinated chloride ions (Cl $2p_{1/2}$ and Cl $2p_{3/2}$). The four XPS peaks at 905.45, 901.17, 887.01, and 882.64 eV can be accredited to the multiple splits of positive trivalent Ce ions (Ce 3d). The XPS peaks at 401.90 and 399.90 eV are due to the nitrogen atom in the chiral cations (N 1s), and the O 1s signal at 533.00 eV originates from the oxygen atom in CH_3OH. Scanning electron microscopy (SEM) and energy dispersive spectroscopy (EDS) mapping were also performed, revealing the uniform elemental distribution with no obvious enrichment (Figures S7 and S9). Moreover, the EDS spectra showed that the ratio of C/Cl/Ce/N atoms was similar to the stoichiometric ratio (12:4:1:1) of *R*/*S*-MCC (Figures S8 and S10), which further confirmed the purity of the as-synthesized RE-based chiral halide samples.

Then, the optical properties of these chiral Ce^{3+}-based halides were investigated *via* UV-visible (UV-vis) diffuse reflectance spectroscopy. As shown in Figure 2a, both *R*-MCC and *S*-MCC exhibit almost identical absorption edges at approximately 354 nm owing to their enantiomeric nature. There are two peaks in the absorption spectra, and the peak located at 260 nm agrees with the absorption of the chiral organic *R*/*S*-MBA cation (Figure S11). Thus, the absorption peak located near 330 nm is attributed to the 4f-5d transition of the Ce^{3+} ion, which is also consistent with the previously reported Ce^{3+} compounds [59–61]. According to the *Tauc* plot, the bandgaps of *R*-MCC and *S*-MCC are approximately 3.53 and 3.54 eV, respectively (Figure S12). The theoretical absorption spectrum of *R*/*S*-MCC was also calculated for comparison by using the frequency-dependent dielectric matrix based on the optimized ground state geometry. The imaginary part of the dielectric tensor is determined by a summation over the empty states, and the real part is obtained by the Kramers-Kronig transformation [62]. The number of empty conduction bands (CBs) is doubled, and the frequency grid points are increased to 2,000 to obtain the reasonable theoretical absorption spectra. As shown in Figure S13, the theoretical absorption spectrum of *R*/*S*-MCC matches thoroughly with the experimental diffuse reflectance absorption spectra. By the introduction of chiral organic cations, the crystal structural symmetry of the Ce^{3+}-based chiral halides decreases, resulting in the unique chiral optical properties. CD refers to the difference in absorption coefficients exhibited by chiral materials to the left- and right-handed circularly polarized light. The CD spectra of *R*-MCC and *S*-MCC were then measured, and the mirror-symmetric signature from 250 to 350 nm was observed, which further confirmed their enantiomeric nature (Figure 2b). In order to clarify the origins of the CD signals of *R*/*S*-MCC, the CD spectra of *R*/*S*-MBA and *R*/*S*-MBACl were measured (Figure S11). The CD signals of *R*/*S*-MCC located near 260 nm corresponded to *R*/*S*-MBA cations, while the CD signal near 330 nm should be attributed to the 4f-5d transition of the Ce^{3+} ion. Therefore, the chirality of *R*/*S*-MBA was successfully transferred to the inorganic framework. Furthermore, the vibrational circular dichroism (VCD)

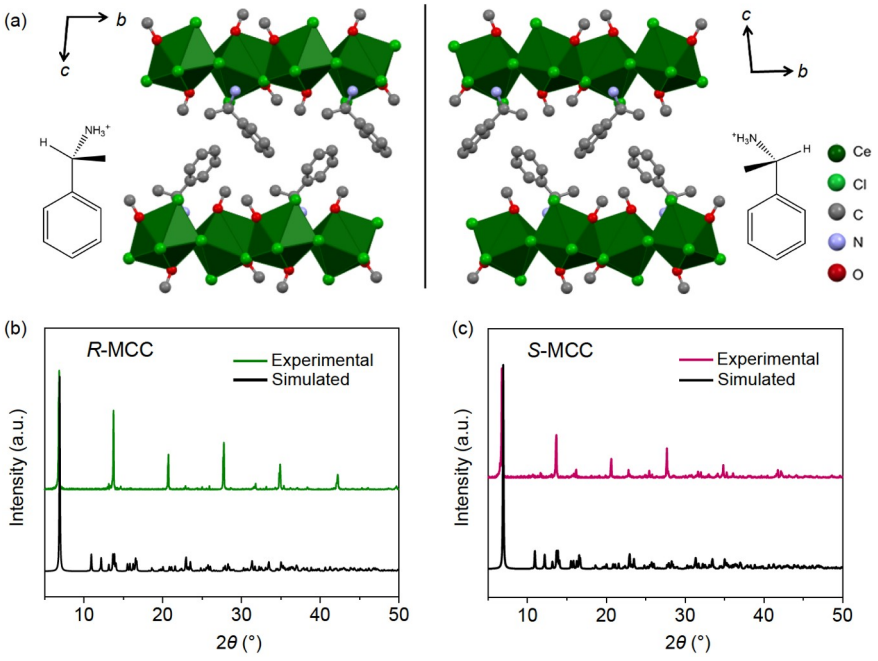

Figure 1 (a) The crystal structures of *R*/*S*-MCC. Ce, Cl, C, N, and O are represented by the dark green, light green, grey, blue, and red spheres, respectively (H atoms are omitted). (b, c) The measured and simulated PXRD patterns of *R*/*S*-MCC (color online).

spectra are measured for *R*/*S*-MCC. As shown in Figure S14, they exhibit the same IR and VCD peaks with opposite signals at the same wavenumbers, which further supports the enantiomorphic structures of *R*- and *S*-MCC.

To further understand the peculiar optical characteristics of *R*- and *S*-MCC, density functional theory (DFT) calculations were performed to explore their optical transitions in detail. The spin-polarized electronic band structure and corresponding partial density of states (PDOS) of the *R*-MCC are shown in Figure 3a, b. There are two valence bands (VBs) near the Fermi level consisting of two unpaired 4f electrons due to the two Ce atoms in the unit cell, while the VBs mainly comprise Cl below the Fermi level. In contrast, the CBs consist of the 4f- and 5d-orbitals of Ce and the p-orbitals of C atoms of the chiral organic cations above the Fermi level. To distinguish the contributions of the chiral cation (*R*/*S*-MBA) and coordinated methanol molecules, as well as the participation of various azimuthal quantum numbers of all atoms, more accurate PDOS analyses of *R*/*S*-MCC were performed and are shown in Figures S15 and S16.

The transition dipole moments (TDMs) between different CBs and VBs within the range from −5.0 to 3.0 eV were calculated. The optical transitions involving VBs consisting of Cl are identified as numbers 1 to 4 in terms of energy from low to high, and their TDMs are one or two orders of magnitude smaller than the transitions using VBs comprising Ce 4f orbitals (Figure S17). The optical transitions constituting Ce 4f orbitals, with TDMs ranging from tens to 210 Debye[2] are labelled 5 to 7 in terms of energy from low to high, show that 4f-5d contributes to the main absorption. In contrast, the contribution of the Cl-Ce transition to the absorption spectrum of these Ce-based halides can be almost neglected. Therefore, the optical properties of RE-based chiral OIHMHs are totally different from that of the traditional chiral OIHMHs based on lead (from halide to lead), and the 4f-related transition dominates the optical properties of RE-based chiral OIHMHs.

To further investigate the influence of Ce^{3+} on the magnetic properties of the *R*/*S*-MCC powders, the temperature-dependent magnetic susceptibility of *R*/*S*-MCC was measured from 2 to 300 K, as shown in Figure 3c. The magnetic susceptibility increases with decreasing temperature throughout the entire temperature range, indicating that *R*/*S*-MCC is paramagnetic, which results from the free spin of the single 4f electron in Ce^{3+} ([Xe]$4f^1$). Due to the strong spin-orbit coupling, the orbital angular momentum and spin magnetic moment jointly determine the magnetic behavior of RE ions. The theoretical effective moments (μ_{cal}) of the typical Hund's rule ions can be calculated as shown in Eq. (1) [63]:

$$\mu_{cal} = g_J\sqrt{J(J+1)}\mu_B \quad (1)$$

where J is the total angular momentum, μ_B is the Bohr magneton, and its g-tensor is defined by the total orbital angular momentum (L) and the total spin angular momentum (S) as g_J=1+[J(J+1)+S(S+1)−L(L+1)]/[2J(J+1)]. The values of all quantum numbers of Ce^{3+} are given in Table S5. The inverse susceptibilities of both *R*- and *S*-MCC exhibit obvious negative curvatures as shown in Figure 3d; this characteristic is considered to be related to the temperature

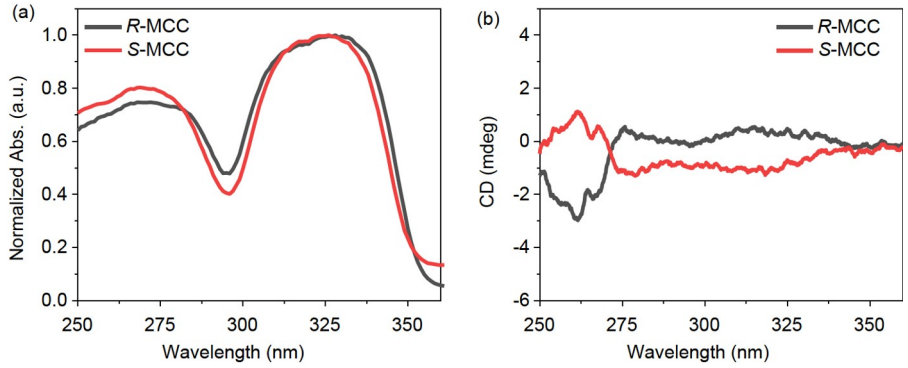

Figure 2 (a) The UV-vis diffuse reflectance spectra of *R*/*S*-MCC. (b) The CD spectra of *R*/*S*-MCC (color online).

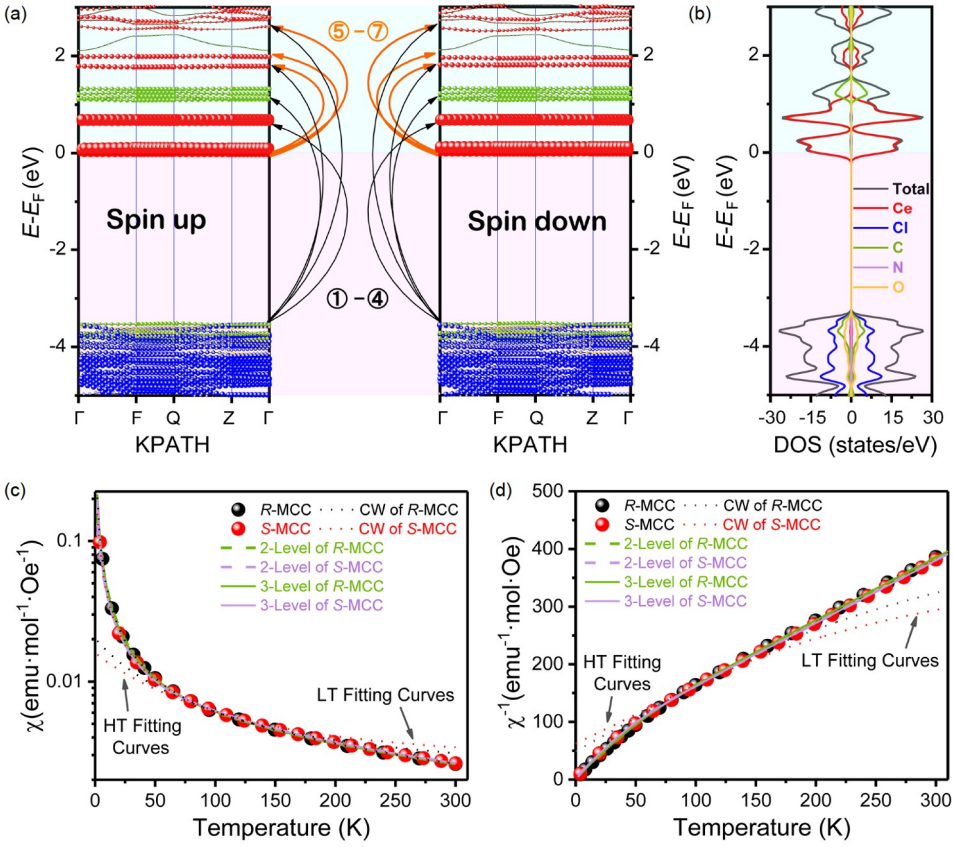

Figure 3 (a) The calculated spin-polarized electronic band structures of *R*-MCC (left panel: spin-up; right panel: spin-down). (b) The spin-polarized partial density of states of *R*-MCC. (c) The temperature dependence of the magnetic susceptibility curves of both *R*-MCC and *S*-MCC in an applied magnetic field of 500 Oe. (d) The temperature dependence of the inverse magnetic susceptibility curves of both *R*-MCC and *S*-MCC in an applied magnetic field of 500 Oe (color online).

independent term (χ_0) in the Curie-Weiss law, as shown in Eq. (2):

$$\chi_m = \frac{C}{T-\theta} + \chi_0 \quad (2)$$

where χ_m represents the magnetic susceptibility, T is the temperature, C is the Curie constant, and θ is the Curie-Weiss temperature [63]. Due to the significant difference between the linear inverse susceptibility above 120 K and the non-linear behaviour below 120 K, we fitted the data in the high temperature (HT, from 120 to 300 K) and low temperature (LT, from 2 to 120 K) ranges. The fitted curves only match with the inverse susceptibility plots within their own temperature ranges and the results are shown in Table S6 [63,64]. The effective magnetic moments (μ_{eff}) of the *R*-MCC and *S*-MCC are calculated by Eq. (3):

$$\mu_{eff} = \sqrt{\frac{3k_B C}{N_A}}\mu_B \approx 2\sqrt{2C}\mu_B[\text{cgs}] \quad (3)$$

where k_B is the Boltzmann constant and N_A is the Avogadro's constant [63]. In the LT region, *R*-MCC and *S*-MCC exhibit significantly underestimated effective magnetic moments of $1.897\mu_B$ and $1.824\mu_B$, respectively. The decrease in the magnetic moment is caused by the thermal depopulation of the excited crystal field levels. In the HT region, slightly higher effective magnetic moments, $2.600\mu_B$ and $2.861\mu_B$, and obvious overestimation of the interaction strengths θ, −41.687 and −63.141 K, are obtained for *R*-MCC and *S*-MCC, respectively. The negative θ values indicate antiferromagnetic coupling between Ce^{3+}, but the plots do not exhibit any long-range ordering, indicating that T_N is less than 2 K. Although T_N is usually smaller than $|\theta|$, for RE ions, the large $|\theta|$ is caused by the thermally populated crystal field levels. In previous studies, the deviation from the Curie-Weiss law was widely observed in Ce-based compounds [63,64]. However, when deviation occurs, a multilevel model under crystal field effects (Eq. (4)) can be used with the effective magnetic moment described by Eq. (5) [64]:

$$\chi^{-1} = 8\cdot(T-\theta)\cdot\frac{1+\sum_{i=1}^{n} e^{\frac{-E_{n-1}}{k_B T}}}{\mu_{\mathrm{eff},0}^2+\sum_{i=1}^{n}\left(\mu_{\mathrm{eff},n-1}^2 e^{\frac{-E_{n-1}}{k_B T}}\right)} \quad (4)$$

$$\mu_{\mathrm{eff}}^2 = \frac{\mu_{\mathrm{eff},0}^2+\sum_{i=1}^{n}\left(\mu_{\mathrm{eff},n-1}^2 e^{\frac{-E_{n-1}}{k_B T}}\right)}{1+\sum_{i=1}^{n} e^{\frac{-E_{n-1}}{k_B T}}} \quad (5)$$

where $\mu_{\mathrm{eff},0}$ is the effective moment of the crystal field ground state, E_{n-1} is the energy between the ground state and the $(n-1)$th excited level and $\mu_{\mathrm{eff},n-1}$ is the effective moment of the excited level. When $n\geqslant 4$, a large number of parameters make the attainment of the *n*-level equation from data fitting complex. We fitted the inverse susceptibilities by 2-level and 3-level equations, and the parameters are listed in Tables S7 and S8. The experimental effective moments of the 2-level equation ($2.499\mu_B$ for *R*-MCC and $2.519\mu_B$ for *S*-MCC) and 3-level equation ($2.497\mu_B$ for *R*-MCC and $2.512\mu_B$ for *S*-MCC) are consistent with the calculated moment μ_{cal} ($2.54\mu_B$). As shown in Figure S18, the difference between the 2-level equation and the 3-level equation lies mainly in the LT region. The difference between the data and the fitted curves indicate that the 3-level equation is more suitable for the susceptibility plots because of the smaller difference from the data at LT (Figure S19). The calculated spin densities of *R*/*S*-MCC are also shown in Figure S20.

To investigate their photoluminescence (PL) properties, PL excitation-emission maps were measured under ambient conditions. As shown in Figure S21, *R*-MCC shows almost the same emission bands at approximately 360 nm under excitation from 220 to 350 nm. The similar PL excitation-emission map of *S*-MCC is obtained owing to the enantiomer nature with *R*-MCC. To avoid the interference from excitation and emission, 303 nm was chosen as the excitation wavelength for the PL measurements. The emission peaks of *R*-MCC and *S*-MCC are almost the same at 356 and 368 nm, which further proves their enantiomeric nature (Figure 4a). According to the calculated electronic structure (Figure 3a, b), the emission peaks in *R*/*S*-MCC may originate from the transition of Ce-5d → Ce-4f. Similar two emission peaks were also observed in other Ce^{3+}-based halides [57]. The excited-state dynamics of *R*-MCC and *S*-MCC were further measured by time-resolved photoluminescence (TR-PL) spectroscopy. As shown in Figure 4b, the fitted PL lifetimes of *R*-MCC and *S*-MCC are 7.3 and 5.6 ns, respectively, which are consistent with the short lifetime of d-f transition luminescence [46,54]. The photoluminescene quantum yield (PLQY) of *R*/*S*-MCC was approximately 11.7±1.0% and 11.3±1.1% (Figure S22). The Commission International de l'Eclairage (CIE) coordinates of *R*-MCC (0.1564, 0.0260) and *S*-MCC (0.1564, 0.0264) are also shown in Figure 4c, clearly indicating that *R*-MCC and *S*-MCC are ideal candidates for circularly polarized light source in the UV region. Therefore, the circularly polarized luminescence (CPL) spectra of *R*-MCC and *S*-MCC were measured. As shown in Figure 4d, the CPL spectra of *R*-MCC and *S*-MCC exhibit mirror-symmetric CPL in the UV region under ambient conditions. The dominant CPL peak located at 360 nm is also very close to the emission peak at 356 nm, further indicating that chirality is successfully transferred from chiral organic cations to the Ce 5d-4f emission peaks of *R*/*S*-MCC. The anisotropy factor of CPL was further calculated based on Eq. (6):

$$g_{lum} = \frac{2(I_L - I_R)}{I_L + I_R} \quad (6)$$

where I_L and I_R refer to the intensity of the left- and right-handed CPL, respectively [65–67]. The calculated $|g_{lum}|$ values are approximately 6.33×10^{-4} and 3.34×10^{-4} at 370 nm for *R*-MCC and *S*-MCC, respectively (Figure S23). Given the current scarcity of CPL materials in the UV region, Ce^{3+}-based chiral OIHMHs exhibit enormous potential for expanding CPL toward the UV region (Scheme 1). Further investigations will be performed to increase both the g_{lum} and PLQY of Ce^{3+}-based chiral OIHMHs towards real applications. The thermal stability and photostability of the samples were also evaluated under different conditions. As shown in Figure S24, under the continuous irradiation with UV light at 348 nm for 120 min, the PL intensity of *S*-MCC was slightly changed, which indicates that *R*/*S*-MCC are photostable. The sample can still emit consistent ultraviolet luminescence before and after being heated at 60 °C for 6 h (Figure S25). Thermogravimetric analysis (TGA) was further performed to evaluate the thermal stability of *R*-MCC. The results showed that *R*-MCC gradually decomposed as the temperature

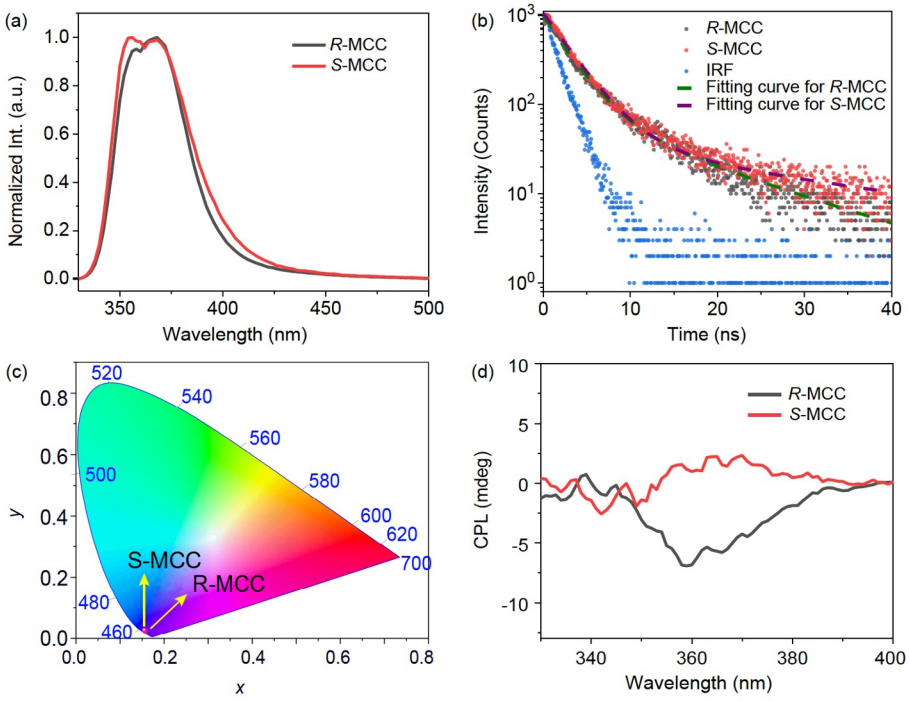

Figure 4 (a) PL emission spectra of *R*/*S*-MCC. (b) PL decay curves of *R*/*S*-MCC. (c) The CIE color coordinate diagram converted from the emission spectra of *R*/*S*-MCC. (d) The CPL spectra of *R*/*S*-MCC (color online).

increased. Starting from ~80 to ~160 °C, two CH_3OH molecules are lost from *R*-MCC, resulting in a weight loss of approximately 13%. As the temperature increases to ~230 and ~315 °C, a total weight loss of 33% is attributable to the sublimation of MBACl. After the subsequent heating process, the residual weight remains almost constant for $CeCl_3$ with a high melting point (848 °C) (Figure S26). The result showed that *R*- and *S*-MCC have good stability against heat and UV irradiation.

In summary, our work reports the first chiral organic-inorganic hybrid metal halide based on the RE element, *R*/*S*-MCC. The obtained chiral cerium halide crystals belong to the *P*1 *Sohncke* space group, and a 1D chain-like structure is formed by the introduction of chiral cations, which surround edge-sharing Ce^{3+}-based dodecahedrons. The chirality is successfully transferred from chiral organic cations to the inorganic RE framework, resulting in the chiral UV light emission from Ce^{3+} ions. The mirror-symmetric CD and CPL spectra were obtained for *R*-MCC and *S*-MCC. Most importantly, the combination of chirality with RE element endows the chiral metal hybrid halides with both paramagnetism and UV CPL emission. Our work promotes the maturation of RE-based chiral metal halides by providing appreciable support for accessing circularly polarized light sources in the UV region. We believe that our work provides a new stage for the development of chiral organic-inorganic hybrid metal halide families. The fusion of RE-based chiral halides with the superior optical, electrical, magnetic, and spintronic features of RE elements with chirality will accelerate the maturation of chiral optoelectronics and spintronics toward real applications.

Acknowledgements This work was supported by the National Natural Science Foundation of China (92256202, 12261131500, 22305129, 22371131, 52103218), the Fundamental Research Funds for the Central Universities, Nankai University (023-63223021), Tianjin Key Lab for Rare Earth Materials and Applications (ZB19500202), the Outstanding Youth Project of Tianjin Natural Science Foundation (20JCJQJC00130), China Postdoctoral Science Foundation (BX20220157, 2022M721698), and the 111 Project (B12015, B18030). All the theoretical calculations were performed at National Supercomputer Center in Guangzhou.

Conflict of interest The authors declare no conflict of interest.

Supporting information The supporting information is available online at http://chem.scichina.com and http://link.springer.com/journal/11426. The supporting materials are published as submitted, without typesetting or editing. The responsibility for scientific accuracy and content remains entirely with the authors.

1 Lin J, Chen D, Yang L, Lin T, Liu Y, Chao Y, Chou P, Chiu C. *Angew Chem Int Ed*, 2021, 60: 21434–21440
2 Peng Y, Liu X, Li L, Yao YP, Ye H, Shang X, Chen X, Luo J. *J Am Chem Soc*, 2021, 143: 14077–14082
3 Ming F, Wu X, Chen C, Wang KD, Mai P, Maier TA, Strockoz J, Venderbos JWF, González C, Ortega J, Johnston S, Weitering HH. *Nat Phys*, 2023, 19: 500–506
4 Wu Z, Zhang W, Ye H, Yao Y, Liu X, Li L, Ji C, Luo J. *J Am Chem Soc*, 2021, 143: 7593–7598
5 Lu H, He T, Wu H, Qi F, Wang H, Sun B, Shao T, Qiao T, Zhang H, Sun D, Chen Y, Tang Z, Long G. *Adv Funct Mater*, 2024, 34: 2308862
6 Zhou S, Li J, Lu J, Liu H, Kim JY, Kim A, Yao L, Liu C, Qian C, Hood ZD, Lin X, Chen W, Gage TE, Arslan I, Travesset A, Sun K, Kotov NA, Chen Q. *Nature*, 2022, 612: 259–265

7 Zhang Z, Wang Z, Sung HHY, Williams ID, Yu ZG, Lu H. *J Am Chem Soc*, 2022, 144: 22242–22250
8 Kim K, Vetter E, Yan L, Yang C, Wang Z, Sun R, Yang Y, Comstock AH, Li X, Zhou J, Zhang L, You W, Sun D, Liu J. *Nat Mater*, 2023, 22: 322–328
9 Jiang S, Kotov NA. *Adv Mater*, 2023, 35: 2108431
10 Rikken GLJA, Raupach E. *Nature*, 1997, 390: 493–494
11 Long G, Jiang C, Sabatini R, Yang Z, Wei M, Quan LN, Liang Q, Rasmita A, Askerka M, Walters G, Gong X, Xing J, Wen X, Quintero-Bermudez R, Yuan H, Xing G, Wang XR, Song D, Voznyy O, Zhang M, Hoogland S, Gao W, Xiong Q, Sargent EH. *Nat Photon*, 2018, 12: 528–533
12 Wang J, Fang C, Ma J, Wang S, Jin L, Li W, Li D. *ACS Nano*, 2019, 13: 9473–9481
13 Zhao Y, Dong M, Feng J, Zhao J, Guo Y, Fu Y, Gao H, Yang J, Jiang L, Wu Y. *Adv Opt Mater*, 2022, 10: 2102227
14 Davydova MP, Meng L, Rakhmanova MI, Bagryanskaya IY, Sulyaeva VS, Meng H, Artem'ev AV. *Adv Opt Mater*, 2023, 11: 2202811
15 Kim YH, Zhai Y, Lu H, Pan X, Xiao C, Gaulding EA, Harvey SP, Berry JJ, Vardeny ZV, Luther JM, Beard MC. *Science*, 2021, 371: 1129–1133
16 Long G, Sabatini R, Saidaminov MI, Lakhwani G, Rasmita A, Liu X, Sargent EH, Gao W. *Nat Rev Mater*, 2020, 5: 423–439
17 Liu Q, Wei Q, Ren H, Zhou L, Zhou Y, Wang P, Wang C, Yin J, Li M. *Nat Commun*, 2023, 14: 7179
18 Ma J, Wang H, Li D. *Adv Mater*, 2021, 33: 2008785
19 Han D, Yang X, Han J, Zhou J, Jiao T, Duan P. *Nat Commun*, 2020, 11: 5659
20 Jin X, Sang Y, Shi Y, Li Y, Zhu X, Duan P, Liu M. *ACS Nano*, 2019, 13: 2804–2811
21 Zhan X, Xu FF, Zhou Z, Yan Y, Yao J, Zhao YS. *Adv Mater*, 2021, 33: 2104418
22 Hao C, Wang G, Chen C, Xu J, Xu C, Kuang H, Xu L. *Nano-Micro Lett*, 2023, 15: 39
23 Zhan X, Zhou Z, Zhou W, Yan Y, Yao J, Zhao YS. *Adv Opt Mater*, 2023, 11: 2200872
24 Banerjee U, Karmakar A, Saha A. *Int J Microw Wireless Technol*, 2020, 12: 922–943
25 Kishi H, Mizuno Y, Chazono H. *Jpn J Appl Phys*, 2003, 42: 1–15
26 Manna E, Fungura F, Biswas R, Shinar J, Shinar R. *Adv Funct Mater*, 2015, 25: 1226–1232
27 Chen C, Gao L, Gao W, Ge C, Du X, Li Z, Yang Y, Niu G, Tang J. *Nat Commun*, 2019, 10: 1927
28 Atzori M, Rikken GLJA, Train C. *Chem Eur J*, 2020, 26: 9784–9791
29 Long G, Adamo G, Tian J, Klein M, Krishnamoorthy HNS, Feltri E, Wang H, Soci C. *Nat Commun*, 2022, 13: 1551
30 Peng H, Liu Q, Liu Y, Lu Y, Liao W. *Chin Chem Lett*, 2023, 34: 107980
31 Xue J, Wang Z, Comstock A, Wang Z, Sung HHY, Williams ID, Sun D, Liu J, Lu H. *Chem Mater*, 2022, 34: 2813–2823
32 Liu D, Li H, Han R, Liu H, Zang S. *Angew Chem Int Ed*, 2023, 62: e202307875
33 Zhu Z, Zhu T, Wu J, You S, Yu P, Liu X, Li L, Ji C, Luo J. *Adv Funct Mater*, 2023, 33: 2214660
34 Fu X, Zeng Z, Jiao S, Wang X, Wang J, Jiang Y, Zheng W, Zhang D, Tian Z, Li Q, Pan A. *Nano Lett*, 2023, 23: 606–613
35 Sun B, Liu XF, Li XY, Zhang Y, Shao X, Yang D, Zhang HL. *Chem Mater*, 2020, 32: 8914–8920
36 Gao JX, Zhang WY, Wu ZG, Zheng YX, Fu DW. *J Am Chem Soc*, 2020, 142: 4756–4761
37 Wang Y, Wang C, Sun M, Zhao P, Fang X, Zhang J, Guo Y, Zhao G. *Adv Opt Mater*, 2023, 2301843
38 Li LS, Tan YH, Wei WJ, Gao HQ, Tang YZ, Han XB. *ACS Appl Mater Interfaces*, 2020, 13: 2044–2051
39 Li B, Rao W, You X, Wang P, Wei J, Wei Z, Zhang H, Cai H. *Inorg Chem*, 2023, 62: 942–949
40 Salah BB, Hajlaoui F, Karoui K, Audebrand N, Roisnel T, Freslon S, Zouari N, Jomni F. *Mater Res Bull*, 2023, 164: 112251
41 Zeng Z, Xu Y, Zhang Z, Gao Z, Luo M, Yin Z, Zhang C, Xu J, Huang B, Luo F, Du Y, Yan C. *Chem Soc Rev*, 2020, 49: 1109–1143
42 Li H, Han K, Li Z, Yue H, Fu X, Wang X, Xia Z, Song S, Feng J, Zhang H. *Adv Sci*, 2023, 2307354
43 Lv R, Raab M, Wang Y, Tian J, Lin J, Prasad PN. *Coord Chem Rev*, 2022, 460: 214486
44 Zheng B, Fan J, Chen B, Qin X, Wang J, Wang F, Deng R, Liu X. *Chem Rev*, 2022, 122: 5519–5603
45 Yi Z, Luo Z, Qin X, Chen Q, Liu X. *Acc Chem Res*, 2020, 53: 2692–2704
46 Zhao Z, Wang L, Zhan G, Liu Z, Bian Z, Huang C. *Natl Sci Rev*, 2021, 8: nwaa193
47 Izuogu DC, Yoshida T, Cosquer G, Asegbeloyin JN, Zhang H, Thom AJW, Yamashita M. *Chem Eur J*, 2020, 26: 6036–6049
48 Nikl M, Yoshikawa A. *Adv Opt Mater*, 2015, 3: 463–481
49 van Loef EVD, Dorenbos P, van Eijk CWE, Krämer K, Güdel HU. *Appl Phys Lett*, 2001, 79: 1573–1575
50 Nikl M, Yoshikawa A, Kamada K, Nejezchleb K, Stanek CR, Mares JA, Blazek K. *Prog Cryst Growth Charact Mater*, 2013, 59: 47–72
51 Xia Z, Meijerink A. *Chem Soc Rev*, 2017, 46: 275–299
52 Li S, Zhou L, Zhang H. *Light Sci Appl*, 2022, 11: 177
53 Ferraro F, Arratia-Pérez R. *Chem Phys Lett*, 2012, 554: 219–224
54 Wang L, Fang P, Zhao Z, Huang Y, Liu Z, Bian Z. *J Phys Chem Lett*, 2022, 13: 2686–2694
55 Shi C, Ye L, Gong Z, Ma J, Wang Q, Jiang J, Hua M, Wang C, Yu H, Zhang Y, Ye H. *J Am Chem Soc*, 2020, 142: 545–551
56 Gu J, Ding Y, Ke J, Zhang Y, Yan C. *Acta Chim Sin*, 2013, 71: 360–366
57 Wang L, Guo Q, Duan J, Xie W, Ji G, Li S, Chen C, Li J, Yang L, Tan Z, Xu L, Xiao Z, Luo J, Tang J. *ACS Energy Lett*, 2021, 6: 4245–4254
58 Jana MK, Song R, Liu H, Khanal DR, Janke SM, Zhao R, Liu C, Valy Vardeny Z, Blum V, Mitzi DB. *Nat Commun*, 2020, 11: 4699
59 Guo R, Wang L, Cai Z, Zhao Z, Bian Z, Liu Z. *Inorg Chem*, 2022, 61: 14164–14172
60 Löble MW, Keith JM, Altman AB, Stieber SCE, Batista ER, Boland KS, Conradson SD, Clark DL, Lezama Pacheco J, Kozimor SA, Martin RL, Minasian SG, Olson AC, Scott BL, Shuh DK, Tyliszczak T, Wilkerson MP, Zehnder RA. *J Am Chem Soc*, 2015, 137: 2506–2523
61 Zhao H, Wang Q, Wen Z, Sun H, Ji S, Meng X, Zhang R, Jiang J, Tang Z, Liu F. *Angew Chem Int Ed*, 2023, 62: e202316336
62 Gajdoš M, Hummer K, Kresse G, Furthmüller J, Bechstedt F. *Phys Rev B*, 2006, 73: 045112
63 Mugiraneza S, Hallas AM. *Commun Phys*, 2022, 5: 95
64 Besara T, Lundberg MS, Sun J, Ramirez D, Dong L, Whalen JB, Vasquez R, Herrera F, Allen JR, Davidson MW, Siegrist T. *Prog Solid State Chem*, 2014, 42: 23–36
65 Zhang C, Li S, Dong X, Zang S. *Aggregate*, 2021, 2: e48
66 Ma J, Fang C, Chen C, Jin L, Wang J, Wang S, Tang J, Li D. *ACS Nano*, 2019, 13: 3659–3665
67 Zhang Y, Yu S, Han B, Zhou Y, Zhang X, Gao X, Tang Z. *Matter*, 2022, 5: 837–875